



Direct N₂O decomposition over iron-substituted small-pore zeolites with different pore topologies

Jong Bin Lim, Seung Hyeok Cha, Suk Bong Hong*

Center for Ordered Nanoporous Materials Synthesis, Division of Environmental Science and Engineering, POSTECH, Pohang, 37673, Republic of Korea



ARTICLE INFO

Keywords:
N₂O decomposition
Fe-substituted PST-7 and LTA zeolites
Steam activation
Zeolite support structure

ABSTRACT

Four cage-based, small-pore zeolites with similar framework Fe contents (0.7–0.9 wt%) but different framework structures (i.e., Fe-PST-7, Fe-LTA, Fe-SSZ-13, and Fe-RTH) have been synthesized and employed as direct N₂O decomposition catalysts. When steam-activated, the light-off temperatures (770 K) for Fe-PST-7 and Fe-LTA were found to be about 40 K lower under wet feed conditions than that (810 K) for Fe-ZSM-5, the most widely studied catalyst for this reaction. Furthermore, their light-off temperatures were found to be even lower than the temperature (780 K) for Fe-FER, the best direct N₂O decomposition catalyst. The overall characterization results of our study strongly suggest that the presence of strong Brønsted acid sites in zeolites, as well as the zeolite framework topology, has a profound effect on the type and distribution of extraframework Fe species, and therefore the N₂O decomposition activity of supported Fe catalysts.

1. Introduction

The emission control of anthropogenic nitrous oxide (N₂O), which is mainly produced as a byproduct of fertilization, fossil fuel and biomass combustion, and industrial chemical processes, has been attracted considerable attention, because of its significant effect on global warming and ozone layer depletion [1–3]. Among various technologies developed so far to solve this problem, the selective catalytic reduction (SCR) of N₂O with reducing agents such as hydrocarbons [4,5] or ammonia [6] and the direct catalytic decomposition of N₂O into N₂ and O₂ have been considered as the most viable [7]. Although direct N₂O decomposition is less effective for removing N₂O at low temperature than SCR, it is economical as no reducing agents are needed. Therefore, the development of catalysts which can more efficiently decompose N₂O in industrial waste gases with typical temperatures of 723 K or lower is of major importance.

Zeolite-supported iron catalysts have been widely investigated as catalysts for direct N₂O decomposition [8–10], because they show an exceptional catalytic performance under practical reaction conditions containing O₂, NO, and SO₂ which severely deteriorate the decomposition activity of other catalysts [11–13]. Among them, Fe ion-exchanged ferrierite (framework type FER) has been regarded as the most active N₂O decomposition catalyst, owing to unique arrangement of two cooperating extraframework Fe²⁺ ions within the 16-hedral ([5⁸6⁶8²]) fer cages where the distance between the two opposing 6-

ring centers is ca. 7 Å [14–17]. Also, the isomorphous substitution of a portion of framework Al by Fe during zeolite synthesis [18,19] has been repeatedly shown to be particularly effective for preparing catalytically more active Fe-containing zeolites for this reaction [11–13,20–22]. This is because the zeolite framework Fe atoms when calcined and steamed at high temperatures can be more easily converted to well-dispersed extraframework oxidic Fe species than the ion-exchanged or sublimed Fe species. We have previously synthesized several Fe-substituted medium-pore zeolites, i.e., Fe-TNU-9 (framework type TUN), Fe-TNU-10 (STI), Fe-IM-5 (IMF), and Fe-ZSM-5 (MFI), and studied their catalytic properties for this reaction [13]. We found that the thermal stability of framework Fe atoms differs according to the zeolite structure, leading to difference in the characteristics and distribution of extraframework Fe species. Thus, the synthesis of new Fe-substituted zeolites provides an opportunity to develop more active catalysts for N₂O decomposition.

Since the great success of Cu-SSZ-13 (CHA) as a commercial NH₃-SCR catalyst [23], as well as of the methanol-to-olefin catalyst H-SAPO-34 with the same framework topology of SSZ-13 [24], much effort has been dedicated to the search for cage-based, small-pore zeolites with new framework topologies and/or compositions. Recent examples of this include the synthesis of high-silica (Si/Al ≥ 8) LTA, PST-7 (UFI), and RTH zeolites [25,26]. To our knowledge, however, no studies have focused on the direct N₂O decomposition over Fe-substituted small-pore zeolites, which is also the case of Fe-substituted FER (Fe-FER) zeolite,

* Corresponding author.

E-mail address: sbhong@postech.ac.kr (S.B. Hong).

Table 1

Crystallographic dimensions of 8-ring windows and cages in Fe-substituted, small-pore zeolites with different cage systems studied here.

Zeolite	IZA Code	Pore dimensionality	8-ring pore size (Å) and area ^{a,b} (Å ²)	Type of cages containing 8-ring windows ^c	Cage dimensions ^a (Å) and volume ^d (Å ³)
Fe-PST-7	UPI	2	4.4 × 3.6, 12.4; 3.3 × 3.3, 8.5	26-hedral ([4 ¹² 6 ⁸ 8 ⁶]) <i>lta</i> cage	11.4 × 11.4 × 11.4, 780
Fe-LTA	LTA	3	4.1 × 4.1, 13.2	26-hedral ([4 ¹² 6 ⁸ 8 ⁶]) <i>lta</i> cage	11.4 × 11.4 × 11.4, 780
Fe-SSZ-13	CHA	3	3.8 × 3.8, 11.3	20-hedral ([4 ¹² 6 ⁸ 8 ⁶]) <i>cha</i> cage	8.4 × 8.4 × 8.2, 300
Fe-RTH	RTH	2	4.1 × 3.8, 12.2; 5.6 × 2.5, 11.0	22-hedral ([4 ⁵ 5 ⁸ 6 ⁴ 8 ⁴]) <i>t-rth</i> cage	10.4 × 11.1 × 9.0, 540

^a Obtained from the Database of Zeolite Structures [27].^b Calculated using the equation $A = \pi ab/4$, where A , a , and b are the pore area and the shortest and longest 8-ring pore diameters, respectively. The eight-ring pores in each material are assumed to be ideally circular or elliptical in shape.^c The windows formed by less than 8 T-atoms and the smaller 8-ring windows of 14-hedral ([4⁵5⁴6⁴8¹]) *wbc* cages in PST-7, where the diffusion coefficients of N₂O with a kinetic diameter of 3.8 Å could not be significant, were not considered here. Also, the very elliptical 8-ring pores (5.6 × 2.5 Å) in RTH were excluded due to the same reason. Thus, RTH should be effectively a 1D small-pore zeolite as far as N₂O decomposition is concerned.^d Calculated using the equation $V = \pi abc/6$, where V , a , b , and c are the cage size and the width, length and height of the cage, respectively. All the cages are assumed to be ideally ellipsoidal in shape.

despite the high activity of Fe ion-exchanged FER for N₂O decomposition [14,15]. Here we report the synthesis of Fe-PST-7, Fe-LTA, and Fe-RTH zeolites, as well as of Fe-SSZ-13, Fe-FER, and Fe-ZSM-5 with similar framework compositions, and the catalytic properties of their proton and steam-activated forms for direct N₂O decomposition. We have also synthesized Fe-free PST-7 and LTA and converted them, together with one commercially available FER (Si/Al = 8.9), to their Fe ion-exchanged form in order to more accurately examine differences in the physicochemical properties of framework and extraframework iron species. The structural features of the four small-pore zeolites studied here, which are available from the Structure Commission of the International Zeolite Association [27], are listed in Table 1, and the physicochemical properties of Fe catalysts supported on these zeolites have been characterized by various analytical tools including Fe K-edge X-ray absorption near edge structure spectroscopy, transmission electron microscopy, ultraviolet-visible spectroscopy, electron spin resonance, IR, ²⁷Al MAS NMR, and temperature-programmed desorption of NH₃.

2. Experimental

2.1. Catalyst preparation

1,2-dimethyl-3-(2-fluorobenzyl)imidazolium, 1,2-dimethyl-3-(4-methylbenzyl)imidazolium, and 1,2,3-trimethylimidazolium hydroxides were prepared following the procedures reported in our previous papers [25,26] and used as organic structure-directing agents (OSDAs) in the synthesis of Fe-PST-7, Fe-LTA, and Fe-RTH, respectively. For comparison, Fe-SSZ-13, Fe-FER, and Fe-ZSM-5 were synthesized using *N,N,N*-trimethyl-1-adamantanammonium, ethylene glycol, and tetrapropylammonium ions as OSDAs, respectively, as described elsewhere [13,21,28,29]. To obtain Fe-substituted zeolites with similar Fe contents, the Si/Fe ratio in the synthesis mixture was fixed to 80. The synthesis mixture compositions and conditions applied to crystallize these zeolites can be found in Supplementary Table S1. As-made zeolites were calcined in air at 823 K for 8 h, refluxed twice in 1.0 M NH₄NO₃ solutions (1.0 g solid per 100 mL solution) at 353 K for 6 h, and calcined again at 823 K for 4 h to convert them into the proton form.

For comparison, some small-pore zeolites were synthesized as the Fe-free aluminosilicate form and converted to the ammonium form as described above. Then, their ammonium form was converted to the Fe ion-exchanged form by refluxing their ammonium form in 0.01 M FeSO₄·7H₂O (99%, Aldrich) solutions, whose pH was adjusted to ca. 3.0, under N₂ flow at 353 K for 3 h, followed by drying at room temperature and calcination in air at 823 K for 8 h [30]. An Fe ion-exchanged FER was prepared using Na_xK-FER (Si/Al = 8.9, Tosoh) as a starting material for ion exchange, following the procedures described above. Steam activation of Fe-containing zeolites was performed following a procedure identical to that in the literature [13,21]. Zeolite

powder was charged into a U-shaped quartz reactor and heated from room temperature to 873 K with He flow (55 mL min⁻¹) at a rate of 2 K min⁻¹. After replacing the He flow with 40% steam in He (55 mL min⁻¹), the reactor was held at this temperature for 5 h. Finally, the steamed samples were cooled down to room temperature under He flow at a rate of 2 K min⁻¹. The as-made, proton, and steam-activated forms of Fe-substituted zeolites were denoted by hyphenating the prefixes *am*, *H*, and *s* to the zeolite names. Also, the suffix letters HS and IE were added in parentheses to differentiate between the zeolite-supported Fe catalysts prepared by hydrothermal synthesis and ion exchange, respectively. For example, the steam-activated form of Fe-PST-7 prepared by hydrothermal synthesis is designated as *s*-Fe-PST-7(HS).

2.2. Catalysis

N₂O decomposition was carried out under atmospheric pressure in a packed-bed flow reactor. Prior to the reaction, 0.5 g of catalyst pellets with 20/30 mesh size were placed inside a 1/4" quartz tube reactor and pretreated with air flow (560 mL min⁻¹) at 823 K for 2 h. After being cooled down to the initial reaction temperature (623 K), a feed gas stream consisting of 1000 ppm N₂O, 4% O₂ in He balance, with or without 10% H₂O present, was fed into the reactor system. The total gas flow rate was kept constant at 560 mL min⁻¹, equivalent to a gas hourly space velocity (GHSV) of 42,000 h⁻¹. The inlet and outlet N₂O concentrations were measured online by a Thermo Nicolet 6700 FT-IR spectrometer with a 2 m gas cell. The reaction rate (*r*) for N₂O decomposition over each catalyst was calculated using the following equation [31]:

$$r (\text{s}^{-1}) = [(C_{\text{N}_2\text{O}} \cdot X_{\text{N}_2\text{O}} \cdot v) / (\text{ML/MW})] \quad (1)$$

where $C_{\text{N}_2\text{O}}$ is the concentration of N₂O (mol L⁻¹) in feed gas stream, $X_{\text{N}_2\text{O}}$ the conversion of N₂O (%), v the volumetric flow rate (L s⁻¹), ML the Fe content on the catalyst (g), and MW the molecular weight of Fe (55.845 g mol⁻¹). The *r* values were calculated using the data for conversions below 15%, where the reaction is plausibly controlled by the surface reaction. The apparent activation energy (E_{app}) was determined from the slope of the Arrhenius plot using a linear regression model.

2.3. Catalyst characterization

Powder X-ray diffraction (XRD) patterns were recorded on a PANalytical X'Pert diffractometer (Cu K α radiation) with an X'Celerator detector. Elemental analysis for Si, Al, and Fe was conducted on a combination of Shimadzu ICPE-9000 inductively coupled plasma and Perkin-Elmer 5000 atomic absorption spectrophotometer. Crystal morphology and average size were examined with a JEOL JSM-6510 scanning electron microscope (SEM). Fe particle size and location

Table 2

Physical properties of Fe-containing zeolite catalysts prepared in this work.

Catalyst	Si/Al ^a	Fe ^a (wt.%)	Si/Fe ^a	Fe/Al ^a	Crystal shape and average size ^b (μm)	BET surface area ^c (m ² g ⁻¹)		
						Total	Microporous	External
Fe-FER(HS)	8.6	0.88	84	0.10	Rectangular plates, 0.6 × 0.6 × 0.1	330 (330)	270 (260)	60 (70)
Fe-ZSM-5(HS)	30	0.96	86	0.36	Spherulites, 5	410 (330)	280 (200)	130 (130)
Fe-PST-7(HS)	12	0.86	84	0.14	Rectangular plates, 0.5 × 0.5 × 2.0	670 (580)	570 (470)	100 (110)
Fe-LTA(HS)	21	0.87	87	0.24	Cubic, 5	720 (640)	660 (570)	60 (70)
Fe-SSZ-13(HS)	23	0.85	87	0.27	Grain-like, 0.1	690 (570)	560 (480)	130 (90)
Fe-RTH(HS)	12	0.70	107	0.12	Cubic, 0.5	710 (620)	590 (520)	120 (100)
Fe-FER(IE)	8.9	0.80	–	0.10	Rectangular plates, 0.7 × 0.7 × 0.1	330 (330)	280 (280)	50 (50)
Fe-PST-7(IE)	11	0.60	–	0.09	Rectangular plates, 0.5 × 0.5 × 2.0	580 (580)	500 (470)	80 (110)
Fe-LTA(IE)	16	0.70	–	0.15	Cubic, 5	690 (660)	630 (590)	60 (70)
Na-Fe-PST-7(HS) ^d	12	0.85	85	0.14	Rectangular plates, 0.5 × 0.5 × 2.0	620	550	70

^a Determined by elemental analysis.^b Determined by SEM.^c Calculated from N₂ adsorption data for the proton form of zeolites. The values in parentheses are the BET surface areas of the steam-activated form of the corresponding zeolites.^d The Na content and Na/Al ratio of this catalyst determined by elemental analysis are 0.85 wt.% and 0.34, respectively.

were determined by a JEOL JEM-2010 transmission electron microscope (TEM) operating at an accelerating voltage of 200 kV. The N₂ sorption experiments were performed on a Mirae SI Nanoporosity-XG analyzer. The chemical compositions, crystal sizes and shapes, and BET surface areas of catalysts studied here are summarized in Table 2.

Ultraviolet-visible (UV-vis) spectra were recorded on a Shimadzu UV-2600 spectrophotometer in diffuse reflectance mode with BaSO₄ as a reference. The spectra were transformed into the Kubelka-Munk function, *F*(*R*). Electron spin resonance (ESR) spectra were measured at room temperature on a Bruker A200 spectrometer, operating with an X-band cavity (9.44 GHz). Prior to ESR analysis, the zeolite samples were placed inside a quartz tube and pretreated under vacuum (10⁻³ Torr) at 373 K for 2 h. A field modulation of 100 kHz and a sweep time of 41 s were used to record the spectra. The *g* values were calibrated with 2,2-diphenyl-1-picrylhydrazyl (DPPH) radical at *g* = 2.0036. The X-ray absorption near edge spectra (XANES) at the Fe K-edge were collected on the 8C beam line at the Pohang Accelerator Laboratory (PAL, Pohang, Korea) using a Si(111) crystal monochromator and ionization chambers. Fe foil was employed for the energy calibration (*E*₀ = 7,112 eV), whereas Fe₂O₃ (99.8%, Aldrich) was used as a reference compound.

IR spectra in the OH region were recorded on a Nicolet 6700 FT-IR spectrometer. Before IR measurements, the self-supporting zeolite catalyst wafers of approximately 13 mg (1.3 cm diameter) were pretreated under vacuum (10⁻⁵ Pa) at 723 K for 2 h inside a home-built IR cell with CaF₂ windows. ²⁷Al MAS NMR spectra were recorded on a Varian Unity Inova 600 spectrometer, with a spinning rate of 22 kHz at a ²⁷Al frequency of 156,326 MHz. The spectra were obtained with an acquisition of 4000 pulse transients, which were repeated with a pulse length of 0.8 μs and a recycle delay of 2.0 s. The amounts of zeolite samples used in ²⁷Al MAS NMR measurements were kept constant in order to accurately monitor changes in the ²⁷Al resonance intensity by calcination or steaming. The ²⁷Al chemical shifts are reported relative to an Al(H₂O)₆³⁺ solution. NH₃ temperature-programmed desorption (TPD) measurements were performed on a fixed-bed, flow-type apparatus attached to a Hewlett-Packard 5890 series II gas chromatograph with a thermal conductivity detector. Details of the TPD runs are given elsewhere [32].

3. Results and discussion

3.1. General characterization

Comparison of the powder XRD patterns of as-made Fe-PST-7(HS), Fe-LTA(HS), Fe-RTH(HS), and Fe-SSZ-13(HS), as well as of as-made Fe-

FER(HS), with those of the aluminosilicate version of the corresponding zeolites in the literature [27] shows that all of them are phase-pure. This is also the case for their proton and steam-activated forms (Supplementary Fig. S1), indicating that the structure of each Fe-substituted small-pore zeolite synthesized here remains stable during the initial calcination at 823 K to remove the OSDAs occluded, the subsequent NH₄⁺ exchange, recalcination, and steaming steps, as further evidenced by the N₂ adsorption data in Table 2. The lack of any X-ray reflections assignable to α-Fe₂O₃ in Supplementary Fig. S1 suggests that the size of iron oxide particles, if generated during calcination and/or steaming, is too small to be detected by powder XRD.

We note that *am*-Fe-ZSM-5(HS) and *am*-Fe-RTH(HS) underwent a color change from white to pale brown upon conversion to their proton form. After steaming, they became dark brown, suggesting that the extent of extraction of zeolite framework Fe atoms is higher in the steam-activated form. While *am*-Fe-SSZ-13(HS) showed no noticeable color change during calcination, but its color turned pale brown after steaming. However, *am*-Fe-PST-7(HS) and *am*-Fe-LTA(HS) gave no significant color change even after steaming at 873 K. Also, although the color of *am*-Fe-FER(HS) became pale brown during conversion to its proton form, no further color was caused by steaming. It has long been reported that Fe-ZSM-5, which contains isolated extraframework Fe as a major Fe species, remains white even after steaming [33]. Therefore, whether the tetrahedral Fe atoms in Fe-substituted zeolites have been extracted during calcination and/or steaming cannot be reasonably estimated from the color change. However, it is clear that not only their thermal stability but also the characteristics of extraframework species formed differs according to the framework structure of Fe-substituted zeolites.

3.2. Catalytic performance

Fig. 1 shows N₂O conversion as a function of temperature in N₂O decomposition over the proton and steam-activated forms of Fe-PST-7(HS), Fe-LTA(HS), Fe-SSZ-13(HS), Fe-RTH(HS), Fe-FER(HS), and Fe-ZSM-5(HS) at 42,000 h⁻¹ GHSV and 1000 ppm N₂O, 4% O₂, and 0 or 10% H₂O in the feed. Table 3 lists the light-off temperature (*T*₅₀) values of these six Fe supported catalysts on zeolites with different framework topologies under dry and wet conditions. Because the Fe contents (0.7–1.0 wt%) of Fe-substituted zeolites synthesized in this work are similar to one another, the catalytic results in Table 3 and Fig. 1 will reflect the effects of the structure type of zeolite supports, as well as of their chemical properties, on the N₂O decomposition activity of zeolite-supported Fe catalysts. These data reveal that the decomposition activity under both dry and wet conditions increases in the order H-Fe-

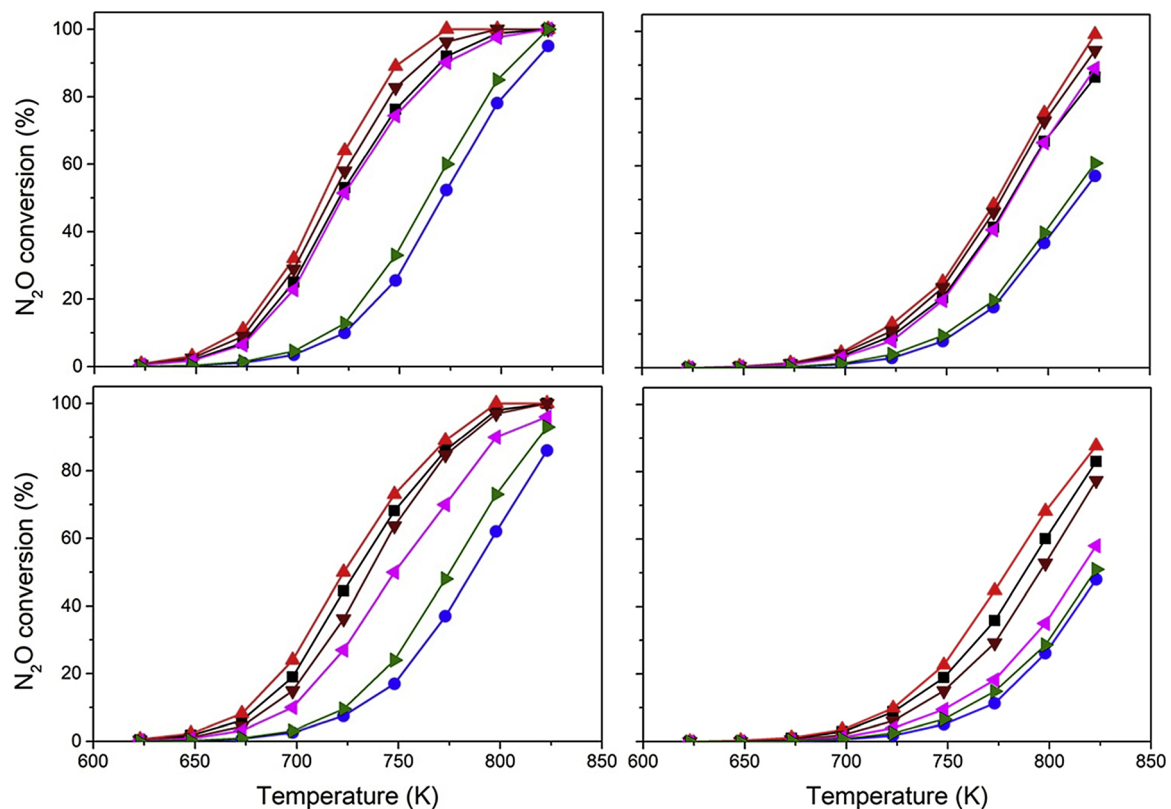


Fig. 1. N₂O conversion as a function of temperature in N₂O decomposition over the proton (bottom) and steam-activated (top) forms of Fe-FER(HS) (■), Fe-ZSM-5(HS) (●), Fe-PST-7(HS) (▲), Fe-LTA(HS) (▼), Fe-SSZ-13(HS) (◆), and Fe-RTH(HS) (▲) under dry (left) and wet (right) feed conditions. The feed contains 1000 ppm N₂O, 4% O₂, and 0 or 10% H₂O balanced with He at 42,000 h⁻¹ GHSV.

ZSM-5(HS) < H-Fe-RTH(HS) < H-Fe-SSZ-13(HS) < H-Fe-LTA(HS) ≈ H-Fe-FER(HS) < H-Fe-PST-7(HS). A similar trend was also observed for their steam-activated analog. Since all these Fe-substituted small-pore zeolites are more active than the channel-based, medium-pore zeolite Fe-ZSM-5(HS), the most widely studied and best characterized catalyst for this reaction [11–13,20–22], it is clear that the sizes of their 8-ring windows (Table 1) are large enough to allow the free diffusion of N₂O molecules with a kinetic diameter of 3.8 Å in the reaction temperature region studied.

Table 3 also shows that the T_{50} values (770 K) of both *s*-Fe-PST-7(HS) and *s*-Fe-LTA(HS) are lower by 40 K than the values (810 K) of *s*-Fe-ZSM-5(HS) under wet feed conditions and are even lower by 10 K

than those (780 K) of *s*-Fe-FER(HS) and *s*-Fe-FER(IE), where the latter catalyst is known to be more active than any of the earlier zeolite-supported Fe catalysts for N₂O decomposition [14–16]. This suggests the high potential of the former two zeolites as N₂O decomposition catalysts. We note here that *s*-Fe-PST-7(IE) and *s*-Fe-LTA(IE) also show lower T_{50} values than *s*-Fe-ZSM-5(HS) under both dry and wet conditions (Supplementary Fig. S2). The r values for N₂O decomposition over the proton and steam-activated forms of the four Fe-substituted small-pore zeolites with different cage systems and of Fe-FER(HS) and Fe-ZSM-5(HS) are compared in Fig. 2. Although they are characterized by similar Fe contents (0.7–1.0 wt%), the r values are larger in the order Fe-ZSM-5(HS) < Fe-RTH(HS) < Fe-SSZ-13(HS) < Fe-FER(HS) ≈ Fe-

Table 3

Catalytic performance of a series of Fe-containing zeolite catalysts with different framework topologies for N₂O decomposition.

Catalyst	$T_{50}^{\text{dry a}}$ (K)		$T_{50}^{\text{wet a}}$ (K)		ΔT_{50}^{b} (K)		$E_{\text{app}}^{\text{dry c}}$ (kJ mol ⁻¹)		$E_{\text{app}}^{\text{wet c}}$ (kJ mol ⁻¹)		$r^{\text{dry d}} \times 10^4$ (s ⁻¹)		$r^{\text{wet e}} \times 10^4$ (s ⁻¹)	
	H-form	s-form	H-form	s-form	dry	wet	H-form	s-form	H-form	s-form	H-form	s-form	H-form	s-form
Fe-FER(HS)	730	720	790	780	10	10	178	180	180	181	3.3	3.7	4.6	5.0
Fe-ZSM-5(HS)	790	770	820	810	20	10	180	178	180	179	0.4	0.6	0.9	1.4
Fe-PST-7(HS)	720	710	780	770	10	10	182	181	181	181	4.4	6.0	5.3	7.0
Fe-LTA(HS)	730	710	790	770	20	20	181	181	181	180	2.4	4.8	3.3	6.0
Fe-SSZ-13(HS)	750	720	810	780	30	30	179	179	182	178	1.8	3.6	2.2	4.4
Fe-RTH(HS)	770	760	820	810	10	10	179	180	178	179	0.7	1.0	1.7	2.7
Fe-FER(IE)	740	730	790	780	10	10	181	181	178	181	2.7	3.2	4.5	4.9
Fe-PST-7(IE)	760	750	810	800	10	10	180	180	181	180	1.6	1.9	3.2	3.5
Fe-LTA(IE)	740	730	790	780	10	10	181	181	180	180	2.7	3.1	4.6	5.0
Na-Fe-PST-7(HS)	750	–	800	–	–	–	178	–	179	–	2.1	–	2.4	–

^a Light-off temperature under dry or wet feed conditions.

^b $\Delta T_{50} = T_{50}(\text{H-form}) - T_{50}(\text{s-form})$.

^c Calculated from the slope of the Arrhenius plot for N₂O decomposition.

^d Determined at 673 K.

^e Determined at 723 K.

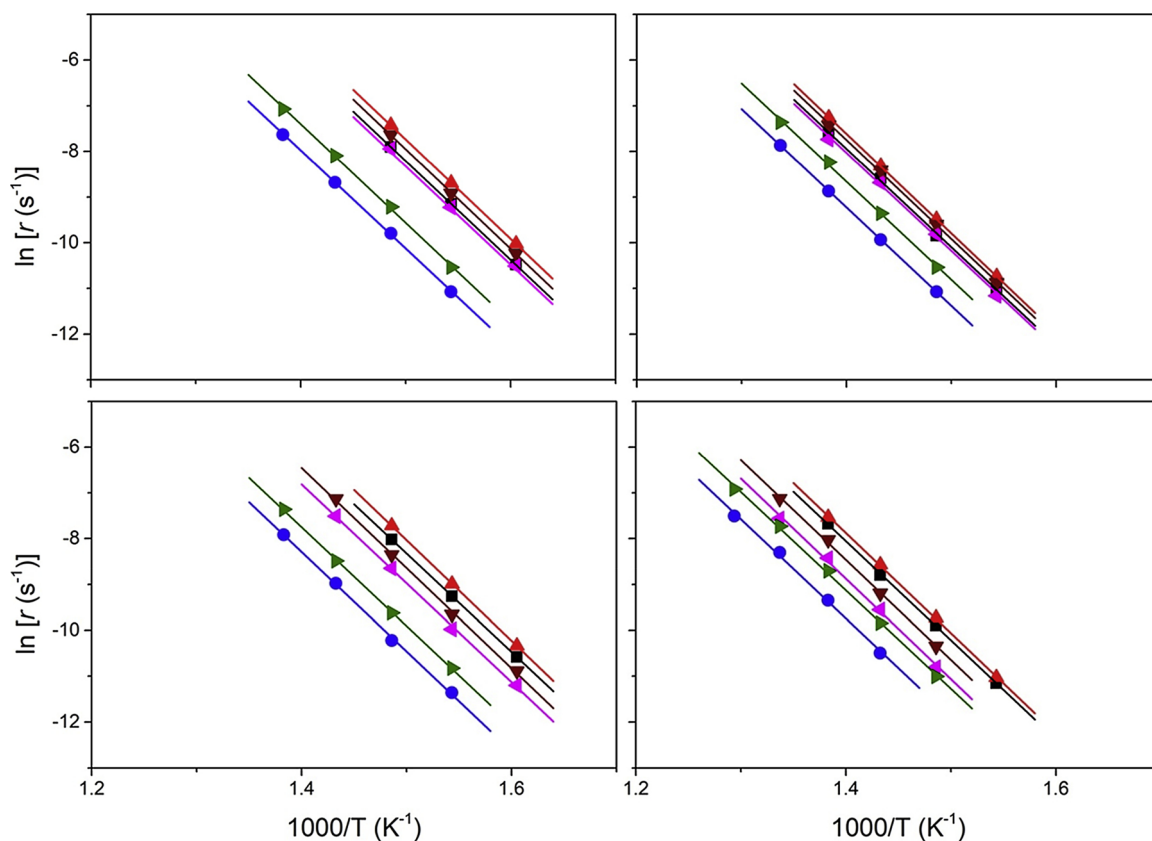


Fig. 2. Reaction rate (r) values for N_2O decomposition over the proton (bottom) and steam-activated (top) forms of Fe-FER(HS) (■), Fe-ZSM-5(HS) (●), Fe-PST-7(HS) (▲), Fe-LTA(HS) (▼), Fe-SSZ-13(HS) (◀), and Fe-RTH(HS) (▶) under dry (left) and wet (right) feed conditions.

$\text{LTA}(\text{HS}) < \text{Fe-PST-7}(\text{HS})$, irrespective of steam activation and the presence of water vapor in the feed gas stream. This suggests that the effect of zeolite topology on the N_2O decomposition activity of supported Fe catalysts is stronger than that of extraframework Al species. As shown in Table 3, in addition, there are no significant differences in the E_{app} values ($178\text{--}182\text{ kJ mol}^{-1}$). It thus appears that the characteristics of active sites in these Fe-containing zeolites for N_2O decomposition may be similar to one another, whereas their number varies considerably with the structure type of zeolite supports and increases upon steaming.

3.3. Physical state of supported Fe species

Fig. 3 shows the Fe K-edge XANES spectra of the as-made, proton, and steam-activated forms of six Fe-substituted zeolites with different framework structures. For comparison, the spectra of Fe ion-exchanged FER, PST-7, and Fe-LTA, as well as Fe_2O_3 and Fe foil, are also included because their Fe-substituted analogs (i.e., Fe-FER(HS), Fe-PST-7(HS), and Fe-LTA(HS)) are the three most active N_2O decomposition catalysts among the zeolite-supported Fe catalysts employed here (Fig. 1). All the XANES spectra of as-made Fe-substituted zeolites exhibit a distinct pre-edge peak around 7114 eV due to the $1s \rightarrow 3d$ electronic transition. As shown in Fig. 3, the intensity of this pre-edge peak is significantly weaker in the spectra of their proton and steam-activated forms. The pre-edge peak intensity for tetrahedrally coordinated Fe^{3+} ions in the zeolite framework is well established to be fairly stronger than that for extraframework Fe^{3+} ions in octahedral symmetry, because of the symmetrically forbidden $A_{1g} \rightarrow T_{2g}$ electronic transition in the latter species [34–36]. Therefore, most, if not all, of the Fe species in as-made Fe-substituted zeolites synthesized in this work are located in tetrahedral framework positions. Since the intensity of the pre-edge peak in the XANES spectra of the proton and steam-activated forms of all Fe-

substituted zeolites is essentially the same as that in the spectra of the steam-activated form of Fe-FER(IE), Fe-PST-7(IE), and Fe-LTA(IE), in addition, it is clear that the majority of framework Fe atoms in Fe-substituted zeolites have been converted into extraframework Fe species during calcination and steaming.

Fig. 4 shows the TEM images of the as-made, proton, and steam-activated forms of Fe-FER(HS), Fe-PST-7(HS), Fe-SSZ-13(HS), and Fe-ZSM-5(HS). We did not perform TEM measurements on Fe-LTA(HS) and Fe-RTH(HS) because the catalytic activities of their proton and steam-activated forms, as well as the colors, are very similar to those of the corresponding forms of Fe-PST-7(HS) and Fe-ZSM-5(HS), respectively. No detectable particles were found in the TEM image of *am*-Fe-ZSM-5(HS). As shown in Fig. 4, however, the image of H-Fe-ZSM-5(HS) exhibits a few particles of 3 nm or so. Since the number of such particles is much larger in the image of *s*-Fe-ZSM-5(HS), the extent of extraction of framework Fe atoms and/or that of aggregation or sintering of the resulting extraframework species in Fe-ZSM-5(HS) may be considerably higher during steaming at 873 K . It is interesting to note that H-Fe-FER(HS), H-Fe-PST-7(HS), and H-Fe-SSZ-13(HS), as well as their steam-activated form, show no detectable particles. This suggests that the formation of Fe_xO_y aggregates, whose diameters are larger than zeolite cavities or channels, is considerably more difficult in Fe-FER(HS), Fe-PST-7(HS), and Fe-SSZ-13(HS) than in Fe-ZSM-5(HS).

Fig. 5 shows the UV-vis spectra of a series of zeolite-supported Fe catalysts prepared here. The spectra of the as-made form of all Fe-substituted small-pore zeolites except *am*-Fe-RTH(HS) are characterized by two $\text{Fe}^{3+} \leftarrow \text{O}$ charge-transfer (CT) bands at a wavelength of ca. 215 and 250 nm , assignable to the $t_1 \rightarrow t_2$ and $t_1 \rightarrow e$ transitions of isolated framework Fe^{3+} ions, respectively [13,21,37–40]. The spectra of their proton form also exhibited two CT bands, but are broader than those observed for the as-made form of the corresponding zeolites. While one band at $200\text{--}300\text{ nm}$ is attributable to the isolated Fe^{3+} ions

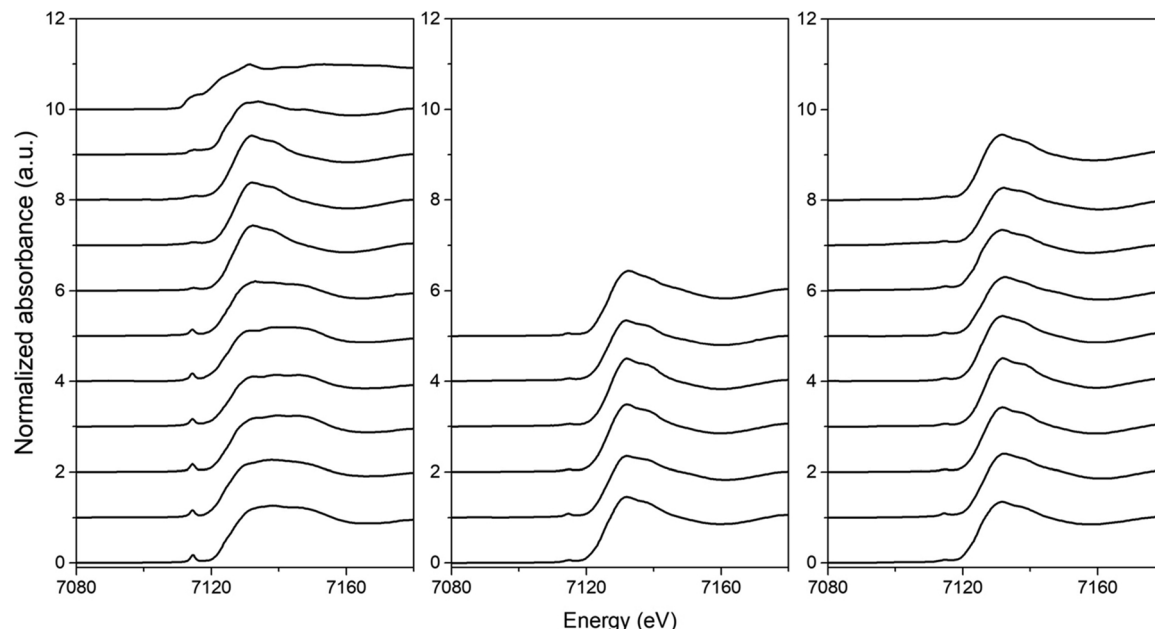


Fig. 3. Fe K-edge XANES spectra of the as-made (left), proton (middle), and steam-activated (right) forms of (from bottom to top) Fe-FER(HS), Fe-ZSM-5(HS), Fe-PST-7(HS), Fe-LTA(HS), Fe-SSZ-13(HS), Fe-RTH(HS), Fe-FER(IE), Fe-PST-7(IE), Fe-LTA(IE), Fe_2O_3 , and Fe foil.

in extraframework positions, the other band at 300–400 nm can be assigned to the small oligonuclear Fe_xO_y clusters formed within zeolite micropores [41–44]. On the other hand, the presence of a weak broad band above 400 nm in the UV-vis spectra of H-Fe-ZSM-5(HS) and H-Fe-RTH(HS) suggests the generation of large Fe_2O_3 particles during calcination. After steam activation, this band becomes more apparent. Comparison of the relative intensities of this broad tail in Fig. 5 reveals that the formation of Fe_xO_y clusters is easier in the order s-Fe-PST-7(HS) \approx s-Fe-LTA(HS) $<$ s-Fe-SSZ-13(HS) \approx s-Fe-FER(HS) $<$ s-Fe-RTH(HS) \approx s-Fe-ZSM-5(HS), in good agreement with the color changes and TEM results (Fig. 4). Therefore, it is most likely that the interactions of extraframework Fe species with the zeolite framework can be altered according to the structure type of zeolite supports and are stronger in Fe-PST-7(HS) and Fe-LTA(HS).

Compared to those of *am*-Fe-FER(HS), *am*-Fe-PST-7(HS), and *am*-Fe-LTA(HS), the UV-vis spectra of Fe ion-exchanged zeolites, i.e., *am*-Fe-FER(IE), *am*-Fe-PST-7(IE), and *am*-Fe-LTA(IE), display considerably broader CT bands in the wavelength region below 400 nm, suggesting the presence of only extraframework Fe species, ranging from isolated Fe^{3+} ions to small oligonuclear Fe_xO_y clusters. Despite the slightly lower Fe contents (0.6–0.8 wt%), in addition, the spectra of s-Fe-FER(IE), s-Fe-PST-7(IE), and s-Fe-LTA(IE) show a slightly stronger CT band above 300 nm than that observed for s-Fe-FER(HS), s-Fe-PST-7(HS), and s-Fe-LTA(HS). This reflects the formation of a relatively larger amount of small oligonuclear Fe_xO_y clusters in the former three zeolites during the aqueous ion exchange and steam activation steps. Therefore, as previously reported [11], the hydrothermal synthesis route may be more efficient for generating well-dispersed isolated extraframework Fe species in zeolite pores than the aqueous ion exchange route.

Fig. 6 shows the ESR spectra of the as-made, proton, and steam-activated forms of Fe-containing zeolites with different pore structures employed in this study. While the ESR line shapes of all six as-made Fe-substituted zeolites are almost the same as one another, the signal at $g = 4.2$ has been repeatedly reported to be due to the isolated Fe^{3+} ions in both framework and extraframework positions [13,21,37]. Because the signal at $g = 2.0$ is assignable to the framework Fe^{3+} ions, as well as to the iron oxide species including small oligonuclear Fe_xO_y clusters and large Fe_2O_3 particles, ESR spectroscopy when used alone has limitations in accurately identifying the Fe species in zeolites. However, the above

Fe K-edge XANES and UV-vis results corroborate the isomorphous substitution of Fe in the framework of as-made Fe-substituted zeolites. Thus, the two signals at $g = 2.0$ and 4.2 in their ESR spectra can be assigned to the framework Fe^{3+} ions in slightly and highly distorted tetrahedral coordinations, respectively.

Fig. 6 also shows that the ESR line shapes of the proton form of Fe-substituted zeolites are quite similar to those of *am*-Fe-FER(IE), *am*-Fe-PST-7(IE), and *am*-Fe-LTA(IE), ascertaining the extraction of framework Fe^{3+} ions into extraframework positions during calcination. The signal at $g = 2.0$ almost disappears, and there is a new less intense signal at $g = 4.2$ that can be ascribed to the isolated extraframework Fe^{3+} ions, as already evidenced by XANES and UV-vis analyses (Figs. 3 and 5). We note here that the ESR line shapes and intensities of s-Fe-PST-7(HS) and s-Fe-LTA(HS) are nearly identical to those of their proton form, unlike the other four Fe-substituted zeolites, especially Fe-ZSM-5(HS). This suggests that the isolated extraframework Fe^{3+} ions in these two cage-based, small-pore zeolites are not much aggregated even after steam activation, which is in line with the TEM and UV-vis results. Therefore, the characterization results confirm the successful partial substitution of Al by Fe in the zeolite framework of Fe-PST-7, Fe-LTA, and Fe-RTH, as well as of Fe-SSZ-13, during hydrothermal synthesis. They also demonstrate that the strength of interactions between extraframework Fe species and zeolite framework, and thus the extent of formation of Fe_xO_y clusters depend intrinsically on the framework topology of zeolite supports.

3.4. Acidic properties of Fe-containing zeolites

Fig. 7 shows the IR spectra in the OH region of the proton and steam-activated forms of Fe-FER(HS), Fe-ZSM-5(HS), Fe-PST-7(HS), Fe-LTA(HS), Fe-SSZ-13(HS), and Fe-RTH(HS). The spectra of the proton form of both Fe-free FER with Si/Al = 8.8 and Al-free Fe-FER with Si/Fe = 16 were reported to exhibit one OH band at 3603 cm^{-1} corresponding to Brønsted acid sites (BASs; bridging Si–OH–Al or Si–OH–Fe groups), respectively [45,46]. As shown in Fig. 7, the spectrum of our H-Fe-FER(HS) exhibits a BAS band at essentially the same position (3603 cm^{-1}). On the other hand, the IR spectra of the proton form of Fe-free ZSM-5 with Si/Al = 35 and Al-free Fe-ZSM-5 with Si/Fe = 49 were reported to exhibit one OH band at 3610 cm^{-1} and

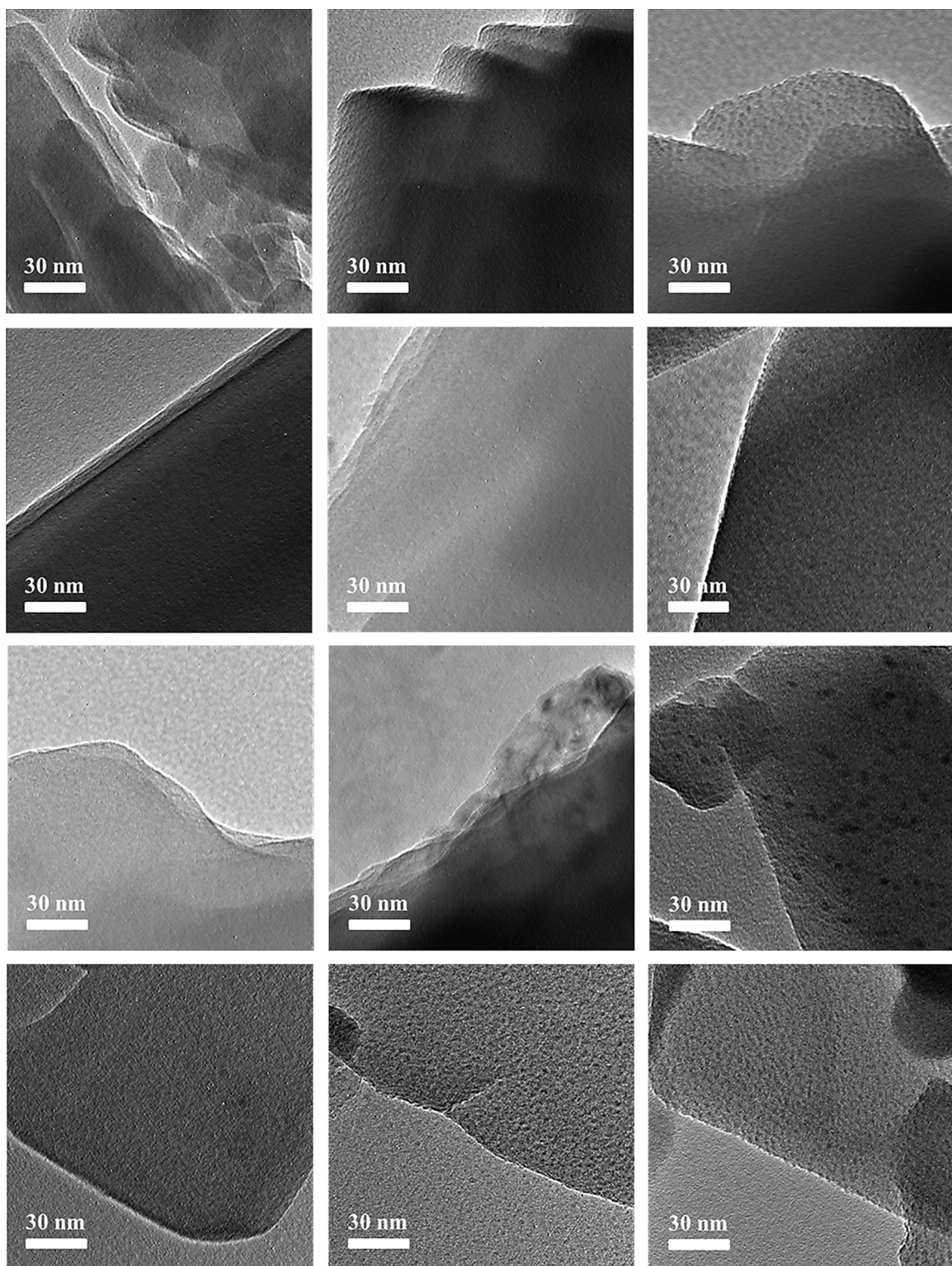


Fig. 4. TEM images of the as-made (left), proton (middle), and steam-activated (right) forms of (from bottom to top) Fe-FER(HS), Fe-ZSM-5(HS), Fe-PST-7(HS), and Fe-SSZ-13(HS).

3630 cm^{-1} corresponding to BASs, respectively [18]. The spectrum of our H-Fe-ZSM-5(HS) displays a BAS band at 3612 cm^{-1} , probably due to the partial extraction of framework Fe during its preparation (Figs. 3 and 6), as well as to the fairly larger Al content than Fe content (Fe/Al = 0.36; Table 2). This can explain why the positions of the high- and low-frequency BAS bands of H-Fe-LTA(HS) and H-Fe-SSZ-13(HS) are similar to those observed for the proton form of Fe-free aluminosilicate

LTA and SSZ-13 zeolites [47,48]. As is expected from its framework structure, the spectrum of H-Fe-PST-7(HS) also shows two IR bands around 3615 and 3560 cm^{-1} that can be assigned to the bridging OH groups pointing to the 26-hedral ($[4^{12}6^88^6]$) *lta* and 14-hedral ($[4^55^46^48^1]$) *wbc* cages, respectively. Unlike the proton form of the other three small-pore zeolites, however, the IR spectrum of H-Fe-RTH (HS) is characterized by one strong BAS band around 3600 cm^{-1} .

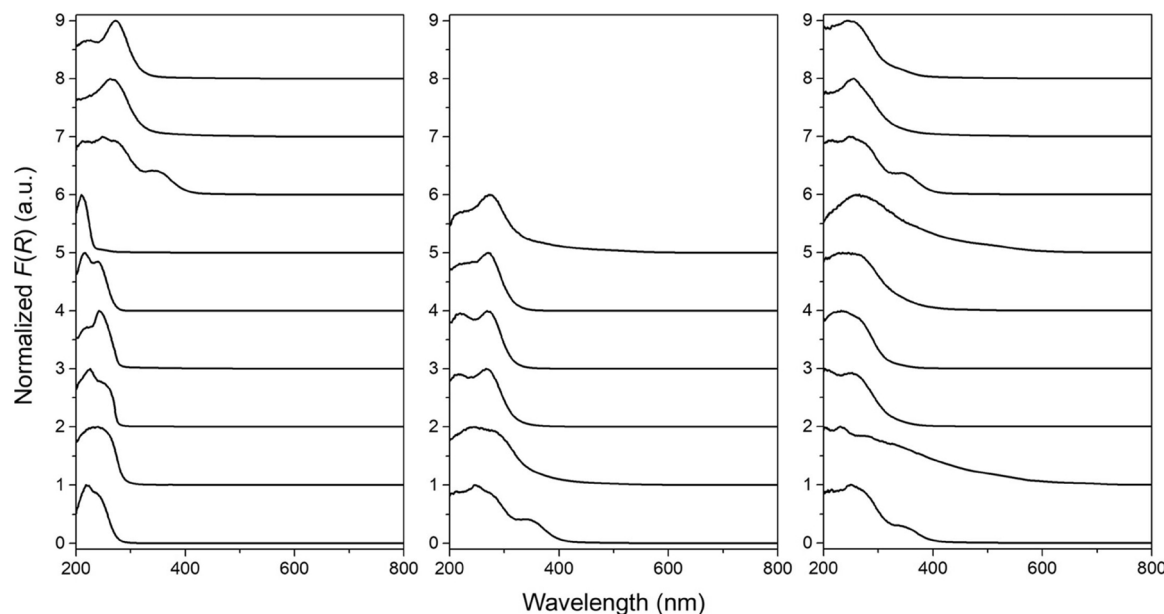


Fig. 5. UV-vis spectra of the as-made (left), proton (middle), and steam-activated (right) forms of (from bottom to top) Fe-FER(HS), Fe-ZSM-5(HS), Fe-PST-7(HS), Fe-LTA(HS), Fe-SSZ-13(HS), Fe-RTH(HS), Fe-FER(IE), Fe-PST-7(IE), and Fe-LTA(IE).

The most important result from Fig. 7 is that the extent of decrease in BAS band intensity caused by steaming of the proton form of Fe-substituted zeolites becomes higher in the order Fe-PST-7(HS) < Fe-LTA(HS) < Fe-FER(HS) < Fe-SSZ-13(HS) < Fe-ZSM-5(HS) ≈ Fe-RTH(HS). We note that this order is opposite to the order of their r values for N_2O decomposition under both dry and wet conditions (Table 3), when excluding the medium-pore zeolite Fe-ZSM-5(HS), but is in general agreement with the order of dealumination in these catalysts determined from the ^{27}Al MAS NMR results (Table 4 and Supplementary Fig. S4). It has been proposed that the extraframework Al species can stabilize cationic Fe species, rendering it more active for N_2O decomposition [43,44]. As shown in Fig. 2 and Table 3, however, the r value of s-Fe-RTH(HS) with the lowest Si/Al_{EF} ratio (16) and thus the highest degree (74%) of dealumination (Table 4) is the smallest among the steam-activated form of the four Fe-substituted small-pore

zeolites with different cage systems, suggesting the existence of another crucial factor affecting the N_2O decomposition activity of zeolite-supported Fe catalysts. This appears to be reasonable because after steaming Fe-PST-7(HS) and Fe-LTA(HS) show notable increases in r value (Table 3), while giving negligible changes in Si/Al_{EF} ratio. A more quantitative ^{27}Al MAS NMR analysis on various Al species [9] such as framework-associated and extraframework octahedral Al species in Fe-containing zeolites studied here is necessary to elucidate the exact role of extraframework Al species in N_2O decomposition, although the details are beyond the scope of our work.

Fig. 8 shows the NH_3 TPD profiles from the proton and steam-activated forms of Fe-substituted zeolites described above. All the TPD profiles from their proton form display two desorption peaks with maxima in the temperature regions 550–580 and 690–760 K, which can be assigned to NH_3 desorption from weak and strong acid sites,

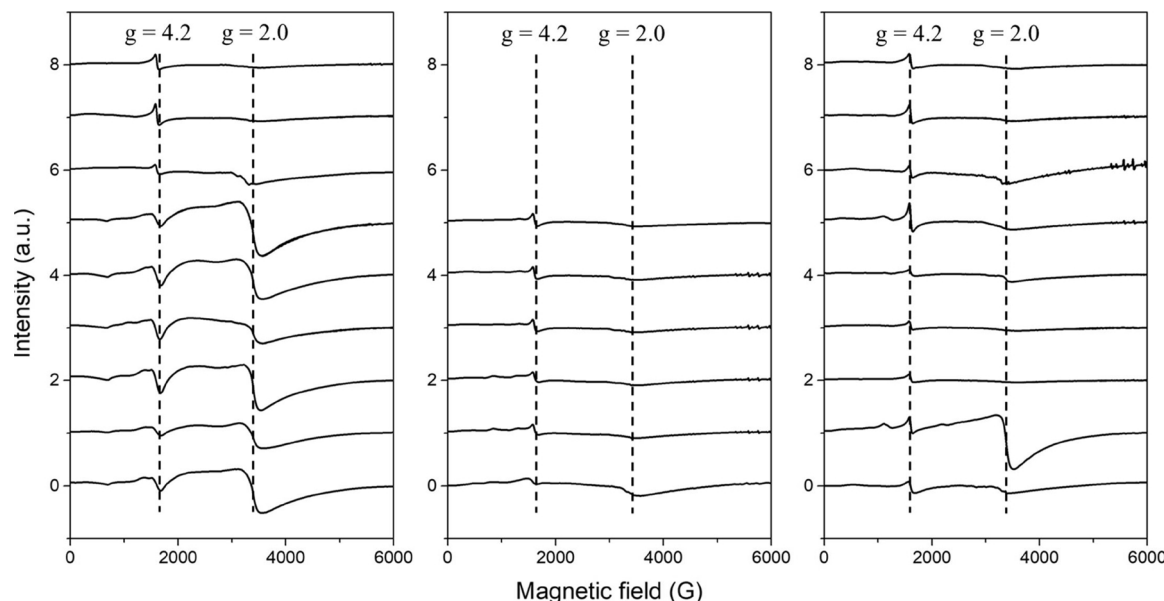


Fig. 6. ESR spectra of the as-made (left), proton (middle), and steam-activated (right) forms of (from bottom to top) Fe-FER(HS), Fe-ZSM-5(HS), Fe-PST-7(HS), Fe-LTA(HS), Fe-SSZ-13(HS), Fe-RTH(HS), Fe-FER(IE), Fe-PST-7(IE), and Fe-LTA(IE).

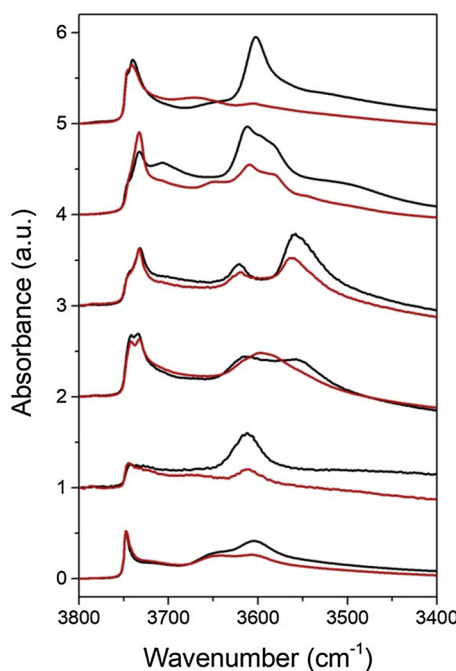


Fig. 7. IR spectra in the 3800–3400 cm^{−1} region of the proton (black) and steam-activated (red) forms of (from bottom to top) Fe-FER(HS), Fe-ZSM-5(HS), Fe-PST-7(HS), Fe-LTA(HS), Fe-SSZ-13(HS), and Fe-RTH(HS) (For interpretation of the references to colour in this figure legend, the reader is referred to the web version of this article).

Table 4

Si/Al_F and Si/Al_{EF} ratios of the proton and steam-activated forms of Fe-substituted zeolites with different framework structures determined by ²⁷Al MAS NMR spectroscopy.

Catalyst	Proton form		Steam-activated form		$\delta_{\text{deAl}}^{\text{b}}$ (%)
	Si/Al _F ^a	Si/Al _{EF} ^a	Si/Al _F ^a	Si/Al _{EF} ^a	
Fe-FER(HS)	17 (8.6)	17	20	15	56
Fe-ZSM-5(HS)	38 (30)	142	138	38	78
Fe-PST-7(HS)	20 (12)	30	21	28	43
Fe-LTA(HS)	38 (21)	47	41	43	49
Fe-SSZ-13(HS)	30 (23)	99	43	49	47
Fe-RTH(HS)	19 (12)	33	46	16	74

^a Al_F and Al_{EF} indicate the framework and extraframework Al atoms, respectively. The values in parentheses are the bulk Si/Al ratios of as-made Fe-substituted zeolites determined by elemental analysis (Table 2). The Si/Al_F and Si/Al_{EF} ratios were calculated using the bulk Si/Al ratio and the relative intensity of the tetrahedral ²⁷Al resonance around 55 ppm in the ²⁷Al MAS NMR spectra of the as-made, proton, and steam-activated forms of Fe-substituted zeolites (Supplementary Fig. S4).

^b Degree of dealumination of steamed Fe-substituted zeolites calculated using the equation $(1 - I_{55,s}/I_{55,am}) \times 100$, where $I_{55,s}$ and $I_{55,am}$ are the relative intensities of the tetrahedral ²⁷Al resonance around 55 ppm in the ²⁷Al MAS NMR spectra of steamed and as-made Fe-substituted zeolites (Supplementary Fig. S4).

respectively. After steaming at 873 K, the high-temperature desorption peak from H-Fe-ZSM-5(HS) and H-Fe-RTH(HS) is hardly observed. As shown in Fig. 8, however, the high-temperature desorption peak from s-Fe-FER(HS), s-Fe-PST-7(HS), and s-Fe-LTA(HS), the three most active N₂O decomposition catalysts among those tested here, is still prominent. This is also the case of s-Fe-SSZ-13(HS), although the relative intensity of its high-temperature desorption peak is slightly weaker than that from the former three catalysts. When combined with the IR results in Fig. 7, therefore, it is most likely that the strong BASs in zeolite-supported Fe catalysts have a beneficial effect on their N₂O

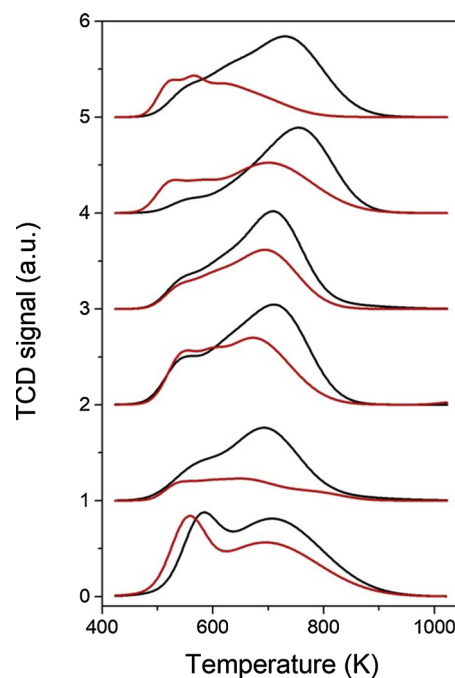


Fig. 8. NH₃ TPD profiles from the proton (black) and steam-activated (red) forms of (from bottom to top) Fe-FER(HS), Fe-ZSM-5(HS), Fe-PST-7(HS), Fe-LTA(HS), Fe-SSZ-13(HS), and Fe-RTH(HS) (For interpretation of the references to colour in this figure legend, the reader is referred to the web version of this article).

decomposition activity.

To check whether the speculation given above is correct, we have prepared Na⁺-exchanged Fe-PST-7(HS), i.e., Na-Fe-PST-7(HS), by refluxing H-Fe-PST-7(HS) in 1.0 M NaNO₃ solutions at 353 K for 6 h and examined its N₂O decomposition activity. Here we selected Fe-PST-7(HS) because its steamed form showed the best N₂O decomposition activity among the catalysts employed here. Elemental analysis reveals that while there are no noticeable differences in the Fe content (0.85 vs 0.86 wt% Fe) of Na-Fe-PST-7(HS) and H-Fe-PST-7(HS), the former catalysts has a Na/Al ratio of 0.34. Deconvolution of the NH₃ TPD results (Supplementary Fig. S5) shows that about 40% of strong acid sites in H-Fe-PST-7(HS) has been removed via Na⁺ exchange. From comparison of the IR spectra in the OH region of these two catalysts (Supplementary Fig. S6), in addition, ca. 70% of the intensity of the two bridging OH bands around 3615 and 3560 cm^{−1} from H-Fe-PST-7(HS) was found to decrease after Na⁺ exchange. Therefore, it is clear that a significant decrease in amount of strong BASs in Fe-PST-7(HS) was caused by Na⁺ exchange. As shown in Table 3 and Supplementary Fig. S7, on the other hand, the T_{50} values (750 and 800 K, respectively) of Na-Fe-PST-7(HS) under dry and wet feed conditions are higher by 30 and 20 K than the values (720 and 780 K, respectively) of H-Fe-PST-7(HS) under corresponding feed conditions, respectively. This led us to conclude that the effect of strong BASs in zeolite supports on the N₂O decomposition activity of zeolite-supported Fe catalysts cannot be ignored, although the BASs in Fe-substituted zeolites cannot directly catalyze this reaction [49]. For example, if BASs contribute to the stabilization of catalytically active extraframework Fe species within zeolite pores via electrostatic interactions, their role can be significant.

4. Conclusions

Fe-PST-7, Fe-LTA, Fe-SSZ-13, and Fe-RTH zeolites with their framework Al partially substituted by Fe, all of which are cage-based, small-pore materials, have been successfully synthesized, and the catalytic properties of their proton and steam-activated forms for N₂O

decomposition have been compared with those observed for the corresponding forms of the channel-based, medium-pore zeolites Fe-FER and Fe-ZSM-5. The reaction rate of these catalysts with similar Fe contents (0.7–1.0 wt%) for N_2O decomposition was found to become higher in the order Fe-ZSM-5 < Fe-RTH < Fe-SSZ-13 < Fe-FER \approx Fe-LTA < Fe-PST-7, whether they are steamed or react with N_2O in the presence of 10% water vapor. Therefore, Fe-LTA and Fe-PST-7 were found to be very attractive as new N_2O decomposition catalysts. A combination of XANES, UV-vis, ESR, IR, and NH_3 TPD results allowed us to conclude that while the type and distribution of extraframework Fe species are greatly influenced by the structure type of zeolite supports, the Brønsted acid sites in zeolites have a positive effect on the N_2O decomposition over supported Fe catalysts.

Acknowledgements

This work was supported by the National Creative Research Initiative Program (2012R1A3A2048833) through the National Research Foundation of Korea. We thank K.-S. Lee (8C, PAL) for help in collecting the X-ray absorption data and PAL for beam time. PAL is supported by MSIP and POSTECH.

Appendix A. Supplementary data

Supplementary material related to this article can be found, in the online version, at doi:<https://doi.org/10.1016/j.apcatb.2018.10.068>.

References

- [1] H. Rodhe, *Science* 248 (1990) 1217–1219.
- [2] A.R. Ravishankara, J.S. Daniel, R.W. Portmann, *Science* 326 (2009) 123–125.
- [3] F. Kapteijn, J. Rodriguez-Mirasol, J.A. Moulijn, *Appl. Catal. B* 9 (1996) 25–64.
- [4] M.C. Campa, D. Pietrogiacomi, M. Occhiuzzi, *Appl. Catal. B* 168–169 (2015) 293–302.
- [5] D. Pietrogiacomi, M.C. Campa, L.R. Carbone, M. Occhiuzzi, *Appl. Catal. B* 240 (2019) 19–29.
- [6] A. Wang, Y. Wang, E.D. Walter, R.K. Kukkadapu, Y. Guo, G. Lu, R.S. Weber, Y. Wang, C.H.F. Peden, F. Gao, *J. Catal.* 358 (2018) 199–210.
- [7] J. Pérez-Ramírez, F. Kapteijn, K. Schöffel, J.A. Moulijn, *Appl. Catal. B* 44 (2003) 117–151.
- [8] P. Sazama, N.K. Sathu, E. Tabor, B. Wichterlová, Š. Sklenák, Z. Sobalík, *J. Catal.* 299 (2013) 188–203.
- [9] I. Melián-Cabrera, E.R.H. van Eck, S. Espinosa, S. Siles-Quesada, L. Falco, A.P.M. Kentgens, F. Kapteijn, J.A. Moulijn, *Appl. Catal. B* 203 (2017) 218–226.
- [10] M. Rutkowska, L. Chmielarz, D. Macina, Z. Piwowarska, B. Dudek, A. Adamski, S. Witkowski, Z. Sojka, L. Obalová, C.J. Van Oers, P. Cool, *Appl. Catal. B* 146 (2014) 112–122.
- [11] J. Pérez-Ramírez, F. Kapteijn, G. Mul, J.A. Moulijn, *Chem. Commun.* (2001) 693–694.
- [12] J. Pérez-Ramírez, F. Kapteijn, G. Mul, J.A. Moulijn, *Appl. Catal. B* 35 (2002) 227–234.
- [13] J.K. Lee, Y.J. Kim, H.-J. Lee, S.H. Kim, S.J. Cho, I.-S. Nam, S.B. Hong, *J. Catal.* 284 (2011) 23–33.
- [14] I. Melián-Cabrera, C. Mentrut, J.A.Z. Pieterse, R.W. van den Brink, G. Mul, F. Kapteijn, J.A. Moulijn, *Catal. Commun.* 6 (2005) 301–305.
- [15] D. Kaucký, Z. Sobalík, M. Schwarze, A. Vondrová, B. Wichterlová, *J. Catal.* 238 (2006) 293–300.
- [16] K. Jíša, J. Nováková, M. Schwarze, A. Vondrová, S. Sklenák, Z. Sobalík, *J. Catal.* 262 (2009) 27–34.
- [17] G. Sádovská, E. Tabor, P. Sazama, M. Lhotka, M. Bernauer, Z. Sobalík, *Catal. Commun.* 89 (2017) 133–137.
- [18] C.T.-W. Chu, C.D. Chang, *J. Phys. Chem.* 89 (1985) 1569–1571.
- [19] J. Čejka, A. Vondrová, B. Wichterlová, G. Vorbeck, R. Fricke, *Zeolites* 14 (1994) 147–153.
- [20] J. Pérez-Ramírez, G. Mul, F. Kapteijn, J.A. Moulijn, A.R. Overweg, A. Doménech, A. Ribera, I.W.C.E. Arends, *J. Catal.* 207 (2002) 113–126.
- [21] J. Pérez-Ramírez, J.C. Groen, A. Brückner, M.S. Kumar, U. Bentrup, M.N. Debbagh, L.A. Villaescusa, *J. Catal.* 232 (2005) 318–334.
- [22] L.V. Pirutko, V.S. Chernyavsky, E.V. Starokon, A.A. Ivanov, A.S. Kharitonov, G.I. Panov, *Appl. Catal. B* 91 (2009) 174–179.
- [23] I. Bull, R.S. Boorse, W.M. Jaglowski, G.S. Koerner, A. Moini, J.A. Patchett, W.-M. Xue, P. Burk, J.C. Dettling, M.T. Caudle, U.S. Patent 0,226,545, 2008.
- [24] P. Tian, Y. Wei, M. Ye, Z. Liu, *ACS Catal.* 5 (2015) 1922–1938.
- [25] D. Jo, J.B. Lim, T. Ryu, I.-S. Nam, M.A. Cambor, S.B. Hong, *J. Mater. Chem. A* 3 (2015) 19322–19329.
- [26] D. Jo, T. Ryu, G.T. Park, P.S. Kim, C.H. Kim, I.-S. Nam, S.B. Hong, *ACS Catal.* 6 (2016) 2443–2447.
- [27] Ch. Baerlocher, L.B. McCusker, Database of Zeolite Structures, <http://www.iza-structure.org/databases/> (Accessed September 21, 2018).
- [28] H.-X. Li, W.E. Cormier, B. Moden, U.S. Patent, 8,541,331, 2013.
- [29] S. Candamano, P. Frontera, T.I. Korányi, A. Macario, F. Crea, J.B. Nagy, *Microporous Mesoporous Mater.* 127 (2010) 9–16.
- [30] F. Gao, M. Kollár, R.K. Kukkadapu, N.M. Washton, Y. Wang, J. Szanyi, C.H.F. Peden, *Appl. Catal. B* 164 (2015) 407–419.
- [31] J.B. Lim, D. Jo, S.B. Hong, *Appl. Catal. B* 219 (2017) 155–162.
- [32] H.J. Jung, S.S. Park, C.-H. Shin, Y.-K. Park, S.B. Hong, *J. Catal.* 245 (2007) 65–74.
- [33] J. Pérez-Ramírez, F. Kapteijn, A. Brückner, *J. Catal.* 218 (2003) 234–238.
- [34] J.A. van Bokhoven, C. Lamberti, *Coord. Chem. Rev.* 277–278 (2014) 275–290.
- [35] G. Berlier, G. Spoto, L. Bordiga, G. Ricchiardi, P. Fisicaro, A. Zecchina, I. Rossetti, E. Sellì, L. Forni, E. Giamello, C. Lamberti, *J. Catal.* 208 (2002) 64–82.
- [36] P. Boroń, L. Chmielarz, J. Gurgul, K. Łątka, T. Shishido, J.-M. Krafft, S. Dzwigaj, *Appl. Catal. B* 138–139 (2013) 434–445.
- [37] G.M. Lari, C. Mondelli, J. Pérez-Ramírez, *ACS Catal.* 5 (2015) 1453–1461.
- [38] A. Ribera, I.W.C.E. Arends, S. de Vries, J. Pérez-Ramírez, R.A. Sheldon, *J. Catal.* 195 (2000) 287–297.
- [39] S. Liu, J. Ren, S. Zhu, H. Zhang, E. Lv, J. Xu, Y.-W. Li, *J. Catal.* 330 (2015) 485–496.
- [40] S. Bordiga, R. Buzzoni, F. Geobaldo, C. Lamberti, E. Giamello, A. Zecchina, G. Leofanti, G. Petrini, G. Tozzola, G. Vlaic, *J. Catal.* 158 (1996) 486–501.
- [41] P. Xie, Y. Luo, Z. Ma, C. Huang, C. Miao, Y. Yue, W. Hua, Z. Gao, *J. Catal.* 330 (2015) 311–322.
- [42] E. Berrier, O. Ovsitser, E.V. Kondratenko, M. Schwidder, W. Grünert, A. Brückner, *J. Catal.* 249 (2007) 67–78.
- [43] J. Wang, H. Xia, X. Ju, Z. Feng, F. Fan, C. Li, *J. Catal.* 300 (2013) 251–259.
- [44] K. Sun, H. Xia, E. Hensen, R. van Santen, C. Li, *J. Catal.* 238 (2006) 186–195.
- [45] A.A. Belhekar, R.K. Ahedi, S. Kuriyavar, S.S. Shevade, B.S. Rao, R. Anand, Z. Tvaruzkova, *Catal. Commun.* 4 (2003) 295–302.
- [46] V. Blasín-Aube, O. Marie, J. Saussey, A. Plesniar, M. Daturi, N. Nguyen, C. Hamon, M. Mihaylov, E. Ivanova, K. Hadjiiyanov, *J. Phys. Chem. C* 113 (2009) 8387–8393.
- [47] T. Ryu, N.H. Ahn, S. Seo, J. Cho, H. Kim, D. Jo, G.T. Park, P.S. Kim, C.H. Kim, E.L. Bruce, P.A. Wright, I.-S. Nam, S.B. Hong, *Angew. Chem. Int. Ed.* 56 (2017) 3256–3260.
- [48] S. Bordiga, L. Regli, D. Cocina, C. Lamberti, M. Bjørgen, K.P. Lillerud, *J. Phys. Chem. B* 109 (2005) 2779–2784.
- [49] J. Pérez-Ramírez, F. Kapteijn, G. Mul, J.A. Moulijn, *Catal. Commun.* 3 (2002) 19–23.